

ARMY RESEARCH LABORATORY



**The Compressive Failure of Aluminum Nitride Considered
as a Model Advanced Ceramic**

by Guangli Hu, K. T. Ramesh, Buyang Cao, and J. W. McCauley

ARL-RP-377

June 2012

A reprint from the *Journal of the Mechanics and Physics of Solids*, Vol. 59, pp. 1076–1093, 2011.

NOTICES

Disclaimers

The findings in this report are not to be construed as an official Department of the Army position unless so designated by other authorized documents.

Citation of manufacturer's or trade names does not constitute an official endorsement or approval of the use thereof.

Destroy this report when it is no longer needed. Do not return it to the originator.

Army Research Laboratory

Aberdeen Proving Ground, MD 21005-5066

ARL-RP-377

June 2012

The Compressive Failure of Aluminum Nitride Considered as a Model Advanced Ceramic

Guangli Hu, K. T. Ramesh, and Buyang Cao
The Johns Hopkins University

J. W. McCauley
Weapons and Materials Research Directorate, ARL

A reprint from the *Journal of the Mechanics and Physics of Solids*, Vol. 59, pp. 1076–1093, 2011.

REPORT DOCUMENTATION PAGE			<i>Form Approved</i> OMB No. 0704-0188	
Public reporting burden for this collection of information is estimated to average 1 hour per response, including the time for reviewing instructions, searching existing data sources, gathering and maintaining the data needed, and completing and reviewing the collection information. Send comments regarding this burden estimate or any other aspect of this collection of information, including suggestions for reducing the burden, to Department of Defense, Washington Headquarters Services, Directorate for Information Operations and Reports (0704-0188), 1215 Jefferson Davis Highway, Suite 1204, Arlington, VA 22202-4302. Respondents should be aware that notwithstanding any other provision of law, no person shall be subject to any penalty for failing to comply with a collection of information if it does not display a currently valid OMB control number. PLEASE DO NOT RETURN YOUR FORM TO THE ABOVE ADDRESS.				
1. REPORT DATE (DD-MM-YYYY) June 2012		2. REPORT TYPE Reprint		3. DATES COVERED (From - To) 2009–2012
4. TITLE AND SUBTITLE The Compressive Failure of Aluminum Nitride Considered as a Model Advanced Ceramic			5a. CONTRACT NUMBER W911NF-06-02-0006	
			5b. GRANT NUMBER	
			5c. PROGRAM ELEMENT NUMBER	
6. AUTHOR(S) Guangli Hu,* K. T. Ramesh,* Buyang Cao,* and J. W. McCauley			5d. PROJECT NUMBER BH 64	
			5e. TASK NUMBER	
			5f. WORK UNIT NUMBER	
7. PERFORMING ORGANIZATION NAME(S) AND ADDRESS(ES) U.S. Army Research Laboratory ATTN: RDRL-WM Aberdeen Proving Ground, MD 21005-5066			8. PERFORMING ORGANIZATION REPORT NUMBER ARL-RP-377	
9. SPONSORING/MONITORING AGENCY NAME(S) AND ADDRESS(ES)			10. SPONSOR/MONITOR'S ACRONYM(S)	
			11. SPONSOR/MONITOR'S REPORT NUMBER(S)	
12. DISTRIBUTION/AVAILABILITY STATEMENT Approved for public release; distribution is unlimited.				
13. SUPPLEMENTARY NOTES A reprint from the <i>Journal of the Mechanics and Physics of Solids</i> , Vol. 59, pp. 1076–1093, 2011. *Department of Mechanical Engineering, The Johns Hopkins University, Baltimore, MD 21218				
14. ABSTRACT Uniaxial quasi-static compression, uniaxial dynamic compression and confined dynamic compression experiments were performed to characterize the failure of Aluminum Nitride (AlN) using a servo hydraulic machine and a modified Kolsky bar set-up respectively. High-speed digital cameras are used to visualize the failure processes. A summary of the available experimental results, including that in the literature, shows that the compressive strength of the AlN is sensitive to strain rate in the range from 10^{-3} to 10^3 s ⁻¹ , and that the deviatoric strength of AlN is linearly dependent on pressure at low pressures and nearly independent of pressure above a transitional pressure (about 2 GPa). TEM characterization of fragments obtained after dynamic loading is used to characterize the deformation mechanisms in the AlN for varying confinement. The transition in the pressure dependent behavior is shown to be the result of a change of deformation mechanism. Classical wing crack micromechanics is used to predict the transition in the deformation mechanism, and to explain the observed behavior at low pressure.				
15. SUBJECT TERMS aluminum nitride, compressive failure, AlN, dynamic, confining stress, failure envelop, deformation mechanism				
16. SECURITY CLASSIFICATION OF:			17. LIMITATION OF ABSTRACT UU	18. NUMBER OF PAGES 26
a. REPORT Unclassified	b. ABSTRACT Unclassified	c. THIS PAGE Unclassified		
			19b. TELEPHONE NUMBER (Include area code) 410-306-0711	



The compressive failure of aluminum nitride considered as a model advanced ceramic

Guangli Hu^a, K.T. Ramesh^{a,*}, Buyang Cao^a, J.W. McCauley^b

^a Department of Mechanical Engineering, The Johns Hopkins University, Baltimore, MD 21218, USA

^b Weapons and Materials Research Directorate, U.S. Army Research Laboratory, Aberdeen Proving Ground, MD 21078, USA

ARTICLE INFO

Article history:

Received 13 December 2010

Accepted 5 February 2011

Available online 15 February 2011

Keywords:

AlN

Dynamic

Confining stress

Failure envelop

Deformation mechanism

ABSTRACT

Uniaxial quasi-static compression, uniaxial dynamic compression and confined dynamic compression experiments were performed to characterize the failure of Aluminum Nitride (AlN) using a servo hydraulic machine and a modified Kolsky bar set-up respectively. High-speed digital cameras are used to visualize the failure processes. A summary of the available experimental results, including that in the literature, shows that the compressive strength of the AlN is sensitive to strain rate in the range from 10^{-3} to 10^3 s⁻¹, and that the deviatoric strength of AlN is linearly dependent on pressure at low pressures and nearly independent of pressure above a transitional pressure (about 2 GPa). TEM characterization of fragments obtained after *dynamic* loading is used to characterize the deformation mechanisms in the AlN for varying confinement. The transition in the pressure dependent behavior is shown to be the result of a change of deformation mechanism. Classical wing crack micromechanics is used to predict the transition in the deformation mechanism, and to explain the observed behavior at low pressure.

© 2011 Elsevier Ltd. All rights reserved.

1. Introduction and background

Engineering ceramics have a wide range of applications that utilize their unique combinations of mechanical, thermal and electrical properties. However, the mechanical response of these materials is complex (in comparison to metals), particularly with respect to the influence of multiaxial stress states and high loading rates, and we lack robust constitutive descriptions that are based on the underlying physics. Increased utilization of engineering ceramics can be expected to go hand-in-hand with the development of better constitutive descriptions for these materials. Motivated by potential applications of such ceramics as armor materials because of their relatively low density, high hardness and high strength, this paper seeks to improve our understanding of the deformation and failure mechanisms in one model ceramic, aluminum nitride (AlN), subjected to dynamic loading under a range of stress states.

Aluminum nitride (Baik and Drew, 1996) is a relatively well-studied engineering ceramic (in comparison to other armor ceramics), and is attractive as a model material because plastic deformation mechanisms have been identified in this ceramic. Single crystal aluminum nitride is a piezoelectric material and a semiconductor, with a wurtzite structure (this is a hexagonal crystal structure that develops spontaneous polarization, and is characteristic of III–V nitrides such as AlN and GaN). The piezoelectric properties of the single crystal are used in a variety of devices, including transducers, microwave filters, MEMS resonators, sensors and actuators (Bu et al., 2004; Dubois and Muralt, 1999; Martin et al., 2000;

* Corresponding author. Tel.: +1 410 516 7735; fax: +1 410 516 7254.

E-mail address: ramesh@jhu.edu (K.T. Ramesh).

Trolier-McKinstry and Muralt, 2004; Zheng et al., 1993). Bulk polycrystalline aluminum nitride is generally not easily poled and so is not used for piezoelectric applications, but has found use in armor applications (Chen et al., 2007; Orphal et al., 1996) both as a standalone material and as part of ceramic composites (particularly with SiC).

Much of the literature on bulk polycrystalline aluminum nitride is motivated by the seminal work of Heard and Cline (1980), who observed an apparent brittle-to-ductile (BD) transition in this material under highly confined compression, and suggested that this brittle-to-ductile transition was correlated to high ballistic performance. This apparent BD transition should not be confused with the true first-order phase transition that is observed in polycrystalline aluminum nitride at very high shock pressures (on the order of 17 GPa): at these pressures the wurtzite structure changes to a rock-salt structure (Branicio et al., 2006; Dandekar et al., 1994; Nakamura and Mashimo, 1994).

Aside from the usual stiffness and hardness measurements, the constitutive response of bulk polycrystalline nitride has been studied in three ways: in terms of quasi-static deformations, high strain rate deformations at low confining pressures and characterizations of the shock behavior (uniaxial strain). Heard and Cline (1980) conducted quasi-static experiments on hot-pressed AlN using jacketed specimens in a fluid-pressurized apparatus at confining stresses as large as 820 MPa, and observed that the peak strength increased with the confining stress. They also observed an apparent brittle to ductile transition at a confining stress of around 550 MPa, which they associated with dislocation motion; this observation triggered a flurry of interest because it suggested that plasticity in ceramics may be a factor during impact events (since these events typically involve high pressures). Chen and Ravichandran (1996) performed dynamic compression tests on sintered AlN at strain rates up to 10^3 s^{-1} , and used a metal sleeve (the “shrink-fit” technique) to apply confining stresses of up to 230 MPa during the dynamic loading. They also found a peak strength that increased with the confining stress, but did not observe a BD transition over their range of confinement. Subhash and Ravichandran (1998) performed uniaxial compression tests (without confinement) on hot-pressed AlN and found that, like many other ceramics (Jiao et al., 2004; Paliwal et al., 2006; Wang and Ramesh, 2004), the compressive strength of aluminum nitride was higher at high strain rates (10^2 – 10^3 s^{-1}) than at low strain rates (10^{-6} – 10^{-2} s^{-1}), with significant rate sensitivity at high rates. Comparison of the data of Chen and Ravichandran (1996) and Subhash and Ravichandran (1998) show that the rate-dependent behavior of the sintered and hot-pressed materials that they examined is similar: compressive strengths on the order of 3 GPa and some rate-sensitivity at high strain rates, with brittle failure mechanisms evident in all cases. Even higher (if non-uniform) strain rates are developed in shock experiments, together with high pressures, and so the rate-dependence and pressure-dependence of the strength can also be examined through characterization of the shock response. Rosenberg et al. (1991) noted that the Hugoniot elastic limit (HEL) of hot-pressed AlN was 9.4 GPa, and measured a *shear* strength of about 3.5 GPa that was nearly independent of the peak shock stress (which is closely related to the pressure) for shock stresses larger than about 10 GPa. Kipp and Grady (1994) also measured the response of hot-pressed AlN to shock loading and identified the phase transformation at about 22 GPa. They also inferred from their experiments that (under this uniaxial strain loading) aluminum nitride deforms plastically at stresses over 9 GPa, but they could make no conclusions on the deviatoric strength. Dandekar et al. (1994) used an equation of state based on diamond-anvil cell experiments to extract the strength from the shock experiments of Grady on aluminum nitride, and concluded that the shear strength of aluminum nitride under shock loading is of the order of 2.8 GPa. In both cases (Kipp and Grady, 1994; Rosenberg et al., 1991), the shear strength was nearly independent of the shock stress for shock stresses above 8.1 GPa, suggesting that plastic deformation mechanisms are active in this ceramic. Note that there has some TEM characterization of the deformation mechanisms under high strain rate loading conditions, e.g., Espinosa et al. (1992). We note that Lankford et al. (1998) concluded that plasticity was a limiting factor in the compressive failure of ceramics by examining Al_2O_3 (and to a lesser extent AlN) over a wide range of strain rates and confinement.

Do the dominant deformation mechanisms in aluminum nitride change with stress state and strain rate? If so, what are the implications for other ceramics? There has long been anecdotal evidence that ceramics flow under high pressures, such as those developed in bearings. Evidence of plastic deformation under pressure has also been provided by Hertzian contact experiments. Understanding the source of such a change in deformation mechanism, if it exists, could provide the opportunity for designing advanced ceramic materials with a much broader range of applications (including in armor). However, none of the previous research on this material has provided visualization of the failure process in real time, and postmortem analysis of failure mechanisms is always difficult in brittle and quasi-brittle solids (given the probability of the growth of cracks even during unloading processes).

This paper presents quasi-static, dynamic and confined dynamic experiments on aluminum nitride used real-time high-speed photography to capture the development of failure processes during loading and unloading. We are thus able to examine the changes of failure processes with strain rate and stress state. We couple these experiments with postmortem TEM characterization to examine microscopic mechanisms, and integrate all of the available data to develop a microphysics-based constitutive description of this ceramic. This also has implications for other brittle solids that may show similar behavior (Chen and Ravichandran, 1997; Heard and Cline, 1980; Lawn et al., 1994; Rhee et al., 2001).

2. Experimental procedures

There are two approaches to the production of bulk polycrystalline aluminum nitride, through liquid phase pressureless sintering (“sintered AlN”) or through hot-pressing (“hot-pressed AlN”) with differences in the microstructure and degree of porosity determined by the processing conditions. We have examined both sintered and hot-pressed AlN, but focused

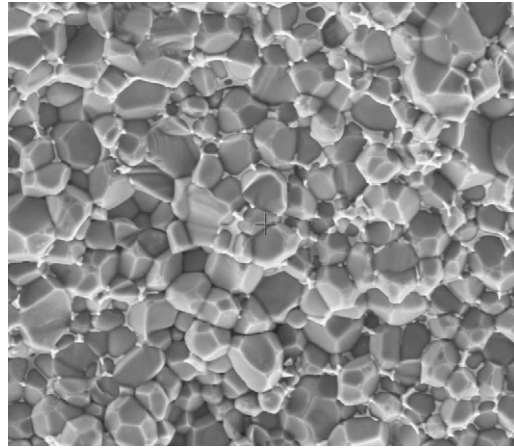


Fig. 1. Field Emission SEM micrograph of a cleaned fractured surface of the sintered AlN showing the average grain size is 5–6 μm . The brighter phase is the yttrium oxide sintering aid and the gray phase is the AlN.

on the sintered AlN in the bulk of this paper. This material is a liquid phase, pressureless sintered AlN, provided by the Dow Chemical Company, with 2% volume fraction of yttria (Y_2O_3) used as a sintering additive (Rafaniello et al.). Fig. 1 presents Field Emission SEM micrograph of a cleaned fracture surface of the as-received sintered AlN, showing that the average grain size is 5–6 μm and that some of grain boundaries are occupied by the sintering additive (yttria). However, not all of the grain boundaries carry yttria: the TEM micrograph of Fig. 2a shows an example of a clean triple junction among the AlN grains, while Fig. 2b and c show regions where the yttria phase sits at triple junctions and sometimes between the AlN grains. Multiple locations have been examined and all of our TEM micrographs indicate that the as-received material is free of dislocations.

The material was obtained in the form of a tile, from which cuboid samples were machined for the experiments. The loading direction was along the thickness direction of the tile. The uniaxial compression samples (both quasistatic and dynamic compression) were square cross-section cuboid specimens with dimensions of 3.6 mm \times 3.6 mm \times 4.0 mm; the loading direction is along the 4.0 mm axis. The confined dynamic compression samples were also cuboids of dimensions 3.5 mm \times 4.0 mm \times 5.3 mm, with the loading direction along the 5.3 mm axis. We characterize the parallelism of the specimen surfaces (critical in the testing of brittle materials) in terms of the lengths along the loading direction at the four corners (defining the largest difference among the lengths as the parallelism tolerance). The parallelism tolerance was less than 3 μm for all of the specimens tested.

2.1. Quasistatic uniaxial compression

An MTS servo-hydraulic test machine was used for the quasistatic uniaxial compression experiments. Tungsten carbide platens jacketed by the Ti-6Al-4V titanium alloy were used to protect the loading surfaces of the testing machine, and the loading surfaces were lubricated. The experiment was performed under displacement control, with a nominal strain rate of 10^{-3} s^{-1} . The cross-head displacement was measured using an LVDT, while the load measurement was obtained from the system load cell. A high resolution Grasshopper (GRAS-20S4M/S) camera was used to record the deformation of the sample at 5 Frames per second, using a Tektronix AFG 3252 function generator to trigger the camera. The camera generated a monitor signal simultaneous with each Frame, and this was used together with a data acquisition card to correlate the stress history with the pictures.

2.2. Dynamic uniaxial compression

The dynamic uniaxial compression tests were performed using a Kolsky bar (sometimes called a split-Hopkinson pressure bar) modified for use with ceramics (Subhash and Ravichandran, 2000; Wang and Ramesh, 2004). A schematic of the overall experimental setup is shown in Fig. 3a. The incident and transmitted bars were 12.7 mm in diameter and 1219 and 1061 mm in length. The bars were made of maraging steel (VascoMax C-350) with a Young's modulus (E) of 200 GPa and density (ρ) 8100 kg/m^3 . Impedance-matched tungsten carbide (LC403, Leech Carbide) platens were jacketed by Ti-6Al-4V sleeves using a shrink-fit technique, and the jacketed platens were inserted between the specimens and the bars to protect the bar surfaces. A spherical joint was added between the tungsten carbide platens and the incident bar to accommodate any lack of parallelism of the specimen, and annealed copper pulse shapers were used to ensure that the specimen achieves stress equilibration before failure occurs.

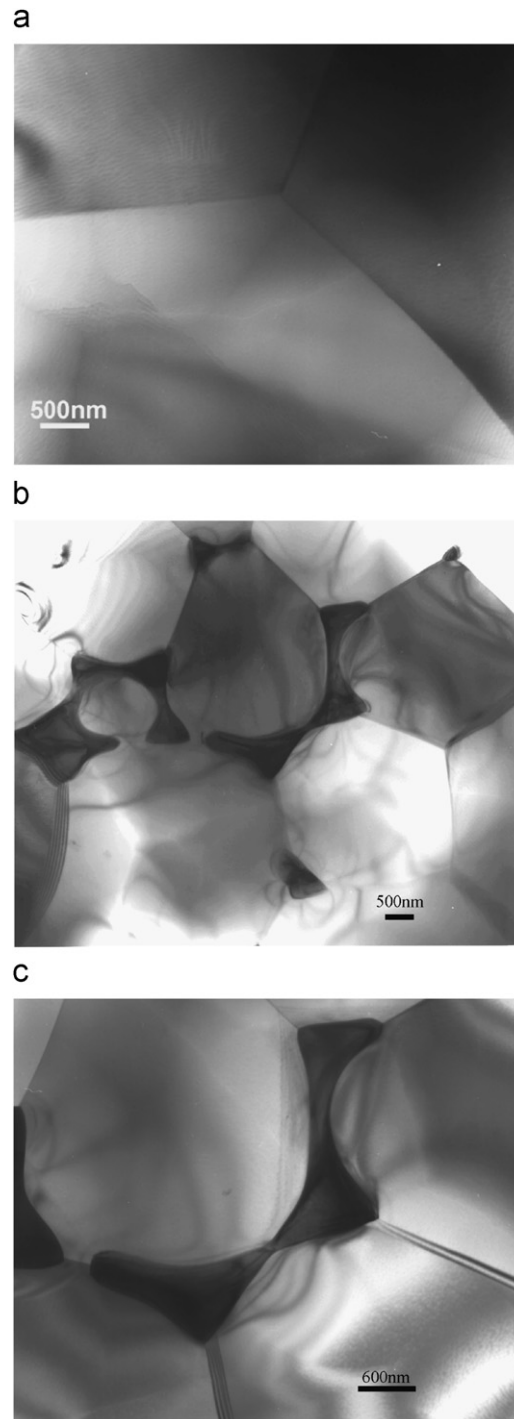


Fig. 2. (a) A clean triple junction in the as-received sintered AlN under TEM. (b) and (c) show regions where the ytria phase sits at triple junctions and sometimes between the AlN grains, respectively. Note the lack of visible dislocations in the as-received material.

An ultra-high-speed DRS Hadland Ultra 8 camera was used to perform real-time visualization of the failure processes in the specimens during the loading and unloading. This camera is capable of capturing up to 8 frames with exposure time as low as 10 ns and a framing rate up to 100 million frames per second. Two Photogenic Powerlight 2500DR flashes were used to provide sufficient lighting during the very short exposures, with the flashes triggered off a separate strain gage (gage 1 in Fig. 3a) on the incident bar. Strain gages 2 and 3 are used for the incident (ϵ_I)/reflected (ϵ_R) and transmitted waves (ϵ_T), respectively. The stress in the specimen can be obtained directly from the transmitted strain pulse using the

equation

$$\sigma = \frac{A_B}{A_S} E \varepsilon_T, \quad (2.1)$$

where A_B , A_S and E are the bar cross-section area, specimen cross-section area and the Young's modulus of the bar, respectively. The strain in the specimen cannot be accurately measured using the stress waves in the bars for the reasons discussed by Wang and Ramesh (2004), among others. Further details on the dynamic uniaxial compression experimental technique as applied to ceramics are also provided in Wang and Ramesh (2004).

2.3. Dynamic confined compression

Paliwal et al. (2008) developed a controlled planar confinement technique, which can be incorporated into Kolsky bar experiments to obtain material properties under multiaxial dynamic loading (with static confinement). In this technique (Fig. 3b), a confining fixture is used to apply quasistatic planar confinement along two of the six faces of a cuboid specimen. The dynamic loading is applied along an orthogonal pair of faces, and the remaining pair of faces is used to obtain the real-time visualization (on one side) and to measure axial strain with an in-situ strain gage (on the side opposite to the camera). The confinement itself is applied through a T-block fixture (Fig. 3b), which uses four tightened bolts to apply the force. A torque wrench is used to apply equal torque incrementally to each bolt so that the confining stress is nominally uniform within the specimen; the system is easily calibrated using a gage block. Annealed titanium alloy cushions are placed between the specimen and the confining fixture to reduce the stress concentrations on the loading surfaces. This part of the specimen assembly is exacting and difficult, with very tight tolerances. The titanium cushions themselves must be polished down to a thickness of 0.7 mm and a mirror surface finish using 0.5 μm diamond paper. We have conducted extensive numerical simulations to study the confined state of the sample with various cushion geometries, and to optimize the loading arrangement (including the evolution of the confining stress during deformation). These simulations and experimental details are provided in Paliwal et al. (2008). The one modification in these experiments is that we now directly measure strain on the specimen using small strain gages. Both axial (along the direction of dynamic loading) and transverse specimen strains have been measured (separately) during such tests. The confining stress can be estimated (*modulo* damage) from the transverse (along the direction of quasistatic confinement) strains directly measured by the strain gage on the specimen before and during dynamic loading.

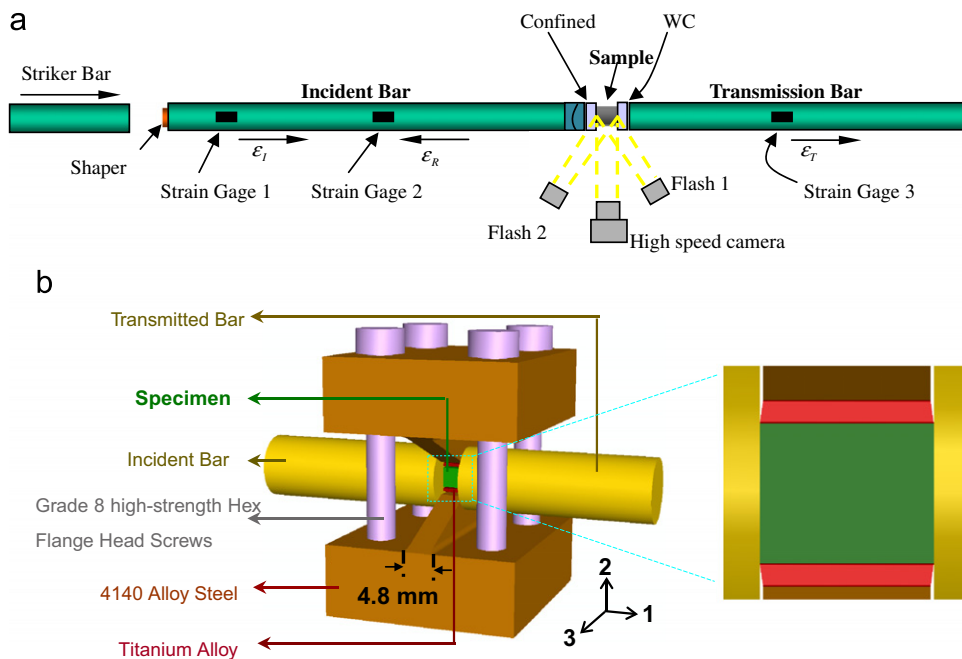


Fig. 3. (a) Modified Kolsky bar experimental set-up for brittle material testing. Note: (i) Pulse shaper, spherical joint and a pair of WC platens are added for the brittle material testing compared to conventional Kolsky bar set-up. (ii) Strain gage 1 is for triggering the camera and strain gages 2 and 3 are used to record the reflected and transmitted signals. The high-speed camera is also shown, together with the flashes. (b) Dynamic confinement compression configuration and the assembly of the specimen. The confining fixture is a pair of T-shaped blocks made of 4140 alloy steel. Four high strength bolts are used to apply the quasi-static confining stress. The cuboid specimen is sandwiched between the fixtures (along the 2 direction). A view of the assembled specimen arrangement is shown on the right. Mirror finished titanium alloy cushions are used between the specimen and the fixture to reduce the stress concentrations. After assembly, the whole fixture is put back into the modified Kolsky bar setup and subjected to dynamic loading (along the 1 direction).

The primary advantage of the planar confinement technique over the shrink-fit confinement technique is that the sample can be observed during the dynamic loading, so that possible changes in failure processes during multiaxial loading can be monitored using ultra-high-speed photography. A secondary advantage is that a very high confining stress can be applied (up to 1 GPa).

3. Experimental results

3.1. Results from uniaxial compression

A representative quasistatic uniaxial compression result is presented in Fig. 4 in terms of the stress history and associated real-time images of the deforming specimen. The stress rate that is obtained from the measured stress history is approximately 200 MPa s^{-1} , corresponding to a nominal strain rate on the order of 10^{-3} s^{-1} . For all of our results, we define the “compressive strength” as the peak stress that is sustained by the specimen during the controlled rate experiments. The compressive strength in the particular experiment shown in Fig. 4a is 3.3 GPa. Once the compressive strength has been reached, the stress in the specimen collapses very rapidly to zero within 10 ms. This quasistatic strength is comparable to that observed by Chen and Ravichandran (1996).

A series of images showing the development of failure in the specimen under quasistatic compression are presented in Fig. 4b; each numbered image is taken at a time indicated by the corresponding marker on the stress–time curve. Since polycrystalline aluminum nitride is opaque, the images only show the surface of the specimen. The loading direction in the images is along the horizontal axis. The progressive damage in the specimen from the onset of loading up to the time of the peak stress is shown in Frames 1–6. The gray region at the center of each frame is the AlN specimen. The initial undamaged state of the specimen is shown in Frame 1. Damage is not observed in the specimen at a stress level of around 1 GPa (Frame 2). Small failures begin to develop at the corners of the specimen as bright spots (see arrows) in Frame 3 at around 2 GPa. One of the corners is beginning to dominate the failure process in Frame 5 (around 3 GPa), and the specimen fails catastrophically at a compressive strength of 3.3 GPa immediately after Frame 6. At later times the specimen has been reduced to a powder. There is no direct evidence of axial splitting in any of these images of the surface of the specimen, although the fragments suggest that major cracks propagate in the loading direction during the catastrophic failure. This “axial splitting” mode of quasistatic compressive failure in brittle solids is well-known (Bombolakis, 1973; Brace and Bombolakis, 1963; Hoek and Bieniawski, 1984; Horii and Nemat-Nasser, 1985; Nemat-Nasser and Horii, 1982), and has been shown to be energetically favorable (Bhattacharya et al., 1998). The development of significant internal damage in the specimen well before a peak strength is reached (Frame 5) is sometimes surprising to the casual observer, but is to be expected in brittle solids (indeed, the softening caused by the damage is necessary for the development of a peak stress). The quasistatic compressive brittle fracture/damage process before the development of the peak stress has been documented most clearly in transparent brittle solids (e.g. by Paliwal et al. (2006) in AlON and Schulson (1990) in ice), but has been observed also in opaque solids, e.g., in geomaterials (Bombolakis, 1973).

The stress-history and corresponding high-speed camera photographs from a representative uniaxial dynamic test are shown in Fig. 5, and the influences of the loading and failure dynamics are immediately evident. Note first that the total

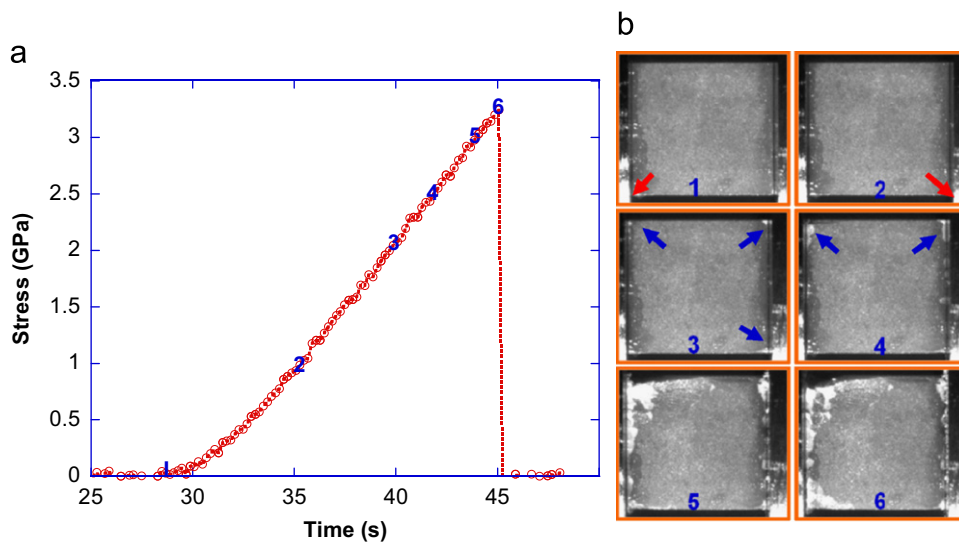


Fig. 4. (a) Quasi-static stress–time history. (b) Images of failure process at different times. Loading is along the horizontal axis. Note (i) Markers on the stress time curves correspond to the images on the right. (ii) White regions in the specimen indicate damaged regions. However, the white regions at the edges of frames 1–6, indicated by the thin arrows above, are the WC platens reflecting light to the camera.

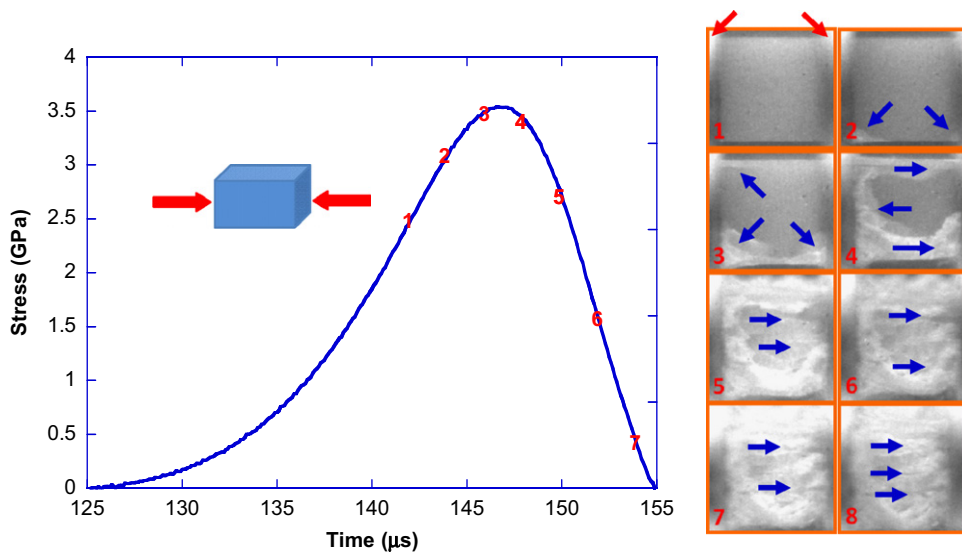


Fig. 5. Stress–time history with high speed camera images of the failure process under uniaxial dynamic compression. Note (i) Inset shows the dynamic loading configuration. (ii) On the right, red arrows show the WC platens and blue arrows shows damage regions and crack propagation.

time shown in the figure is 30 μs . The stress rate for this test is 150 MPa/ μs , corresponding to a nominal strain rate of $\sim 10^3 \text{ s}^{-1}$, six orders of magnitude greater than that in Fig. 4. Next, note that the rate of stress collapse after the peak strength appears gradual at these timescales. This is because we have the time resolution in this experiment to capture the collapse, and because the failure processes within this specimen take time (i.e., the failure dynamics are evident at this time scale). The compressive strength is around 3.5 GPa in this experiment, slightly larger than that observed at the low rates. The markers on the stress–time curve correspond to the high-speed camera Frames pictures on the right hand side of Fig. 5, with exposure times of 200 ns and inter-Frame times of 2 μs . The central region in each Frame is the AlN specimen, and the graded brightness regions on the sides are the WC platens reflecting the light from the flash. The direction of loading is along the horizontal axis. In Frame 1, with the stress level around 2.5 GPa, no apparent failures are observed (failures show up as brighter regions with the lighting arrangement in this experiment). Two microseconds later, at a stress of about 3 GPa, Frame 2 shows that failures have initiated at the bottom left and right corners (see blue arrows). Frame 3 corresponds to a time very close to the peak stress (3.5 GPa) in the stress history, and shows that the damaged region in the lower half of the specimen has grown while a horizontal crack (aligned along the loading direction) has appeared at the top left corner. Note that the bulk of the visible surface is undamaged at the time of the peak stress, but the rate of growth of the damage has accelerated (similar results have been observed during the dynamic failure of other ceramics (Jiao et al., 2004; Paliwal and Ramesh, 2007; Paliwal et al., 2006)). Frame 4, after the compressive strength has been reached, still shows that most of the visible surface is undamaged, although the damaged regions are now contiguous and there is clearer evidence of alignment along the loading direction. Note that the stress at the time of Frame 4 is almost the same as the stress at the time of Frame 3, but the stress rate is now negative, corresponding to the rapid growth of damage. Two microseconds later, in Frame 5, the entire surface has been crossed by failed regions with the appearance of aligned structures that are sometimes referred to as columnar structures (Wang and Ramesh, 2004). The sample is saturated with large horizontal cracks and high crack density regions. This process continues over the next three frames (Frames 6–8), with the cracks interacting and coalescing to form fragments, some of which are so fine that they form a powder.

Several features of the dynamic failure process are of interest. First, the failure process is first visible (Frame 2) on the surface at the corners (the stress concentrations). However, this does not necessarily mean that the failure process inside the specimen begins at the corners, and indeed experiments in transparent solids have shown that the process typically begins at internal flaws during dynamic loading (Paliwal et al., 2006). Second, while cracks are clearly evident, the failure process is relatively diffuse (as in Frame 3), and there is a very large number of cracks that are developed during the 16 μs captured by high speed images in Fig. 5. This is related to the fact that smaller fragments are found after dynamic compression as compared to quasi-static compression; this implies that the nucleation rate is higher in the dynamically loaded case, and that crack interactions are important in the dynamic failure process. Third, the crack velocities are of the order of 1500 m/s while the Rayleigh wave speed in this material is 5820 m/s (i.e., the cracks are moving at least at $\sim 0.25c_R$). Zavattieri and Espinosa (2001) used a cohesive model to demonstrate that crack propagation velocity should be a fraction of the Rayleigh wave speed in ceramics considering the role of material microstructure in terms of grain size and grain distribution (see also the earlier work Espinosa, 1995; Espinosa and Brar, 1995; Espinosa et al., 1992). Fourth, at the time of the peak stress, only about 15% of the specimen surface shows damage (this fraction is always small in dynamically

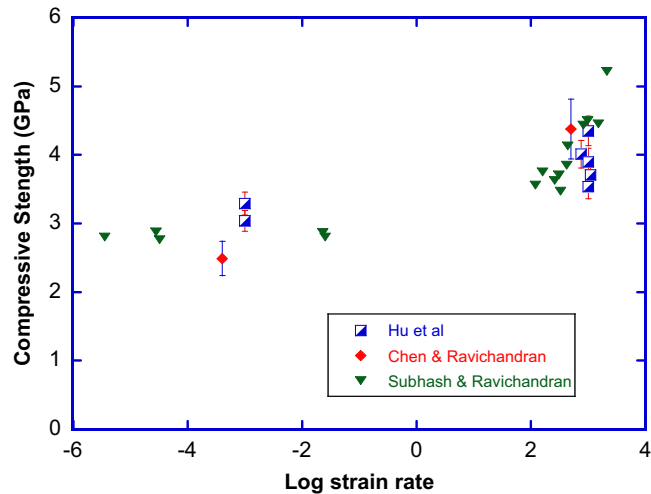


Fig. 6. Effect of strain rate on the compressive strength of AlN. Note that our results and those of Chen and Ravichandran (1996) are for sintered AlN, while those of Subhash and Ravichandran (1998) are for hot-pressed AlN.

loaded ceramics, but varies substantially from material to material (Jiao et al., 2004; Paliwal and Ramesh, 2007; Paliwal et al., 2006)). Finally, substantial lateral dilation of the sample is observed during the stress collapse and is associated with the development of the damage. This effective “bulking” response should be accounted for in constitutive models that include the damage (Holmquist et al., 2001; Paliwal and Ramesh, 2008; Paliwal et al., 2006). Since there is greater nucleation and interaction of cracks during dynamic loading, the bulking response will be greater under high-rate loading than under quasistatic loading. This behavior is not currently incorporated within constitutive models for ceramics.

A comparison of the compressive strength of the aluminum nitride at low and high strain rates demonstrates that this material, like many other ceramics, has higher strain rate dependence of the strength at high strain rates. Our uniaxial compression results on the rate-dependent compressive strength of aluminum nitride are summarized in Fig. 6, together with the data available in the literature (Chen and Ravichandran, 1996; Subhash and Ravichandran, 1998). Error bars are included where available. The general trend towards increased rate dependence of the compressive strength at high strain rates is similar to that observed in many other ceramics (Chen and Ravichandran, 1997; Chen et al., 2007; Jiao et al., 2004; Paliwal and Ramesh, 2007; Paliwal et al., 2006; Ravichandran and Subhash, 1994; Subhash and Ravichandran, 2000; Wang and Ramesh, 2004). This rate dependence has been addressed through several models (Huang and Subhash, 2003; Nemat-Nasser and Deng, 1994; Paliwal and Ramesh, 2007; 2008; Ravichandran and Subhash, 1995), most of which appeal to the inertia associated with dynamic crack growth, although care must be taken into account for experimental artifacts (Ravichandran and Subhash, 1994). Paliwal and Ramesh (2008) demonstrated that the rate-dependent behavior was intimately coupled to the pre-existing distribution of flaws in the ceramic, since this controls the nucleation and interaction of the microcracks. The density of the flaws influences the apparent transition strain rate as well as the strengths that can be achieved (Paliwal and Ramesh, 2008). Note that Fig. 6 includes data on both sintered and hot pressed aluminum nitride, and that the baseline strengths and the rate dependence are comparable, suggesting that the nucleating flaw distributions in the two materials are not very different.

3.2. Results from dynamic confined compression

The dynamic confined compression experiments were designed to allow visualization of the failure process *during* dynamic compressive loading under high planar confinement. The current apparatus is capable of applying confining stresses as high as 1 GPa. Note, however, that the confining stress is first applied in a quasistatic manner, and the dynamic compressive load is subsequently superimposed.

An example of the results of a dynamic confined compression experiment on aluminum nitride is presented in Fig. 7 for a confining stress of 780 MPa. Both the stress history (stress along the dynamic loading direction) and the corresponding high-speed photographs are shown. The duration of the stress pulse is similar to that in Fig. 5, and the form of the stress pulse appears broadly similar to that of the uniaxial compression case. The peak strength is also around 3.5 GPa. The big difference is in the process of specimen failure evident in the high-speed photographs, in that no horizontal cracks are observed in the specimen. The high-speed photographs each have an exposure time of 350 ns, and the interframe time is 2 μ s. The direction of the static confinement is vertical in these pictures, and the direction of dynamic compression loading is horizontal. The titanium alloy cushions can be clearly seen above and below the specimen in each frame. A failure zone is first observed in Frame two, corresponding to a stress (in the horizontal direction) of about 2.2 GPa. Failure zones have nucleated from all the corners by the time of Frame 4. The peak strength occurs at the time of Frame 6, and significant

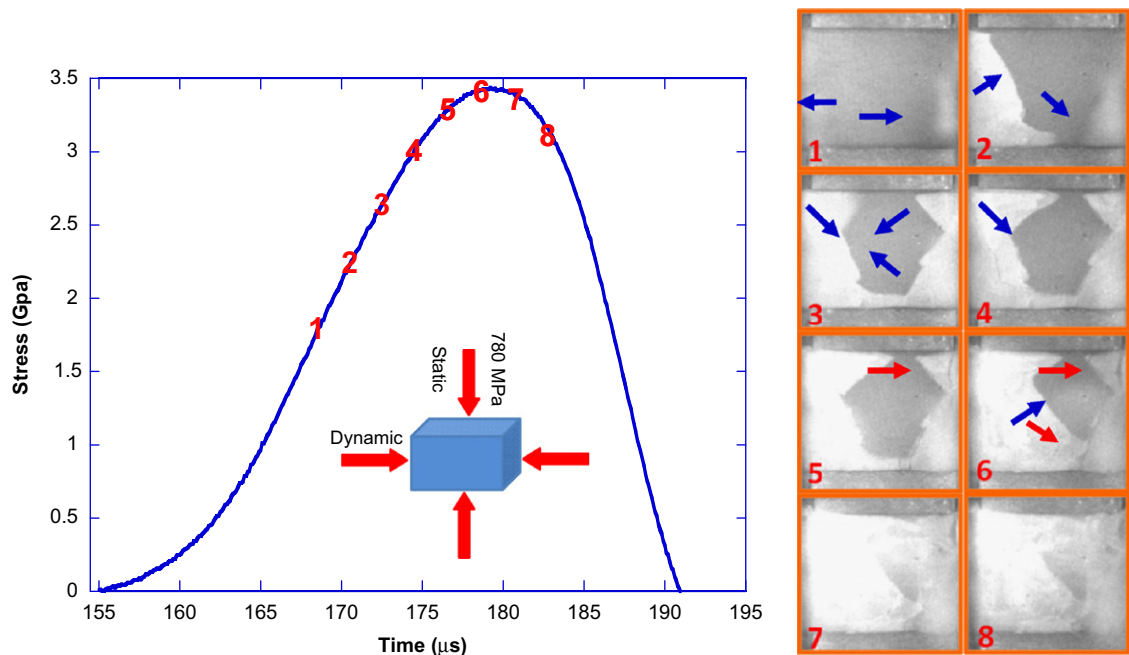


Fig. 7. Stress history and high speed camera images of confined dynamic compression with a confining stress of 780 MPa. Note (i) Inset in the stress-time plot shows the loading condition. (ii) Failure patterns under confined dynamic loading are shear dominated, unlike from uniaxial dynamic loading.

failure has occurred throughout the specimen by Frame 8. However, no horizontal cracks are observed in any of these frames, and indeed no identifiable cracks are visible. The damage appears to develop in diffuse zones that propagate across the specimen along failure fronts that are inclined at about 45° to the dynamic loading direction. This apparently shear dominated failure mode is observed in all of the dynamic confined compression experiments. Thus the presence of the confining stress appears to have dramatically changed the failure mode in this material. The confining stress appears to have suppressed the axial splitting mode, a phenomenon that has been studied in terms of wing crack micromechanics (Horii and Nemat-Nasser, 1986). This change in the macroscopic failure mode can be described, for example, by a multiple-plane microcracking model, which naturally incorporates the damage induced anisotropy (Espinosa, 1995; Espinosa and Brar, 1995). Note that under the confining stress levels (below 780 MPa), cracking is still the dominant deformation mechanism, although some inelastic mechanisms have also been activated (see Section 4). What is observed at the macroscale in our experiments is a macroscopic change in failure mode (from axial splitting in Fig. 5 to the more shear-dominated mode in Fig. 7) because of the change in the collective response of the microcracks under the confining pressures. A similar behavior has been postulated after post-mortem examination of sleeve-confined specimens (Chen and Ravichandran, 1996), but this is the first direct in situ observation of the dynamic evolution of this anisotropic failure process under multiaxial loading.

An interesting and somewhat counterintuitive result from our dynamic confined compression experiments is that the compressive strengths that we measure (3.3–3.8 GPa) in the planar confinement experiments are comparable with (and perhaps even lower than) the compressive strengths (3.6–4.3 GPa) measured in the unconfined cases presented in Fig. 6. This is counterintuitive because most models for the compression of brittle solids would suggest that the strength should increase with confinement (Horii and Nemat-Nasser, 1986; Huang and Subhash, 2003), and this is in fact what was observed by Chen and Ravichandran (1996) on aluminum nitride (using sleeve-based confinement at somewhat lower confining stresses). Why do we not see increased strength at higher confinement in these planar confinement experiments? We hypothesize that this is because of (a) the possibility of relaxation of the stresses due to lack of constraint along the visualization direction and (b) the interaction of the loading path with the pre-existing flaw distribution inside the specimens. The former effect is straightforward from a mechanics perspective: the specimen can expand (both elastically and inelastically) along the unconstrained direction. The latter effect is more subtle: the quasistatic preload in the static confinement can lead to the activation of some of the pre-existing flaws in the material, so that the dynamic loading pulse perceives a material with a different flaw distribution from the virgin material. Here activation means that potential microcrack sites (e.g. carbonaceous inclusions) are triggered under the quasistatic preload. Because of the globally compressive stress state, these cracks are typically of the wing-crack type, and have stress intensity factors that decrease with crack growth as shown by Ashby and Hallam (1986) and subsequently by a number of others; hence, the initial crack growth is stable. This softening mechanism works against the hardening mechanism associated with the confinement, so that we should not expect as much confinement-induced strengthening from the planar confinement experiment as we might expect from a triaxial experiment.

4. Constitutive modeling

We show below that existing models for ceramics do not adequately describe the observed behavior of aluminum nitride, largely because they do not contain the underlying physics of the failure processes that are active in the material. Here we revisit this problem using all of the existing data, our new strength data, and our new real-time visualization of the failure processes, coupled with recently developed micromechanics-based models for compressive brittle failure and microscopic examination of the deformation mechanisms.

The differences in the stress states between the various techniques that produce controlled multiaxial stresses (triaxial/sleeve-based confinement, planar confinement and uniaxial strain/plate impact) are illustrated in Fig. 8. One way to compare the results of these different experiments is to compute the hydrostatic pressures and equivalent stresses generated in each case. The equations for these stresses are listed in Table 1 with the conventions used in Fig. 8. We will refer to the maximum value of the equivalent stress observed in an experiment as the “deviatoric strength” of the material. The experimental results on aluminum nitride from the triaxial/sleeve-based confined experiments (Chen and Ravichandran, 1996) and the planar confinement experiments (this work) can then be compared, as shown in Fig. 9. The deviatoric strength of the aluminum nitride is essentially linearly dependent on the hydrostatic pressure in this pressure range, described quite well by $\sigma_e = -0.23 + 2.82p$. Note that we do not include data from the unconfined (uniaxial stress) compressive experiments, because such a comparison is not meaningful (the ratio of equivalent stress to pressure in the uniaxial stress condition is 3, whatever the material behavior).

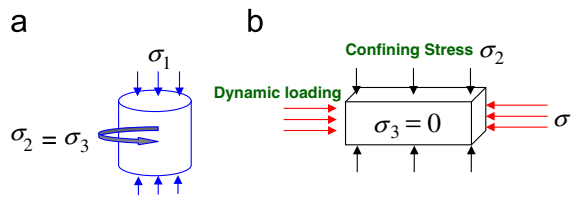


Fig. 8. Stress state corresponding to two confinement techniques (a) shrink fit confinement technique (b) planar confinement technique.

Table 1
Hydrostatic pressure, shear stress and equivalent stress (deviatoric strength) for both techniques.

Shrink-fit confinement technique	Planar confinement technique
$p = \frac{1}{3}(\sigma_1 + 2\sigma_2)$	$p = \frac{1}{3}(\sigma_1 + \sigma_2)$
$\tau = \frac{1}{2}(\sigma_1 - \sigma_2)$	$\tau = \frac{1}{2}\sigma_1$
$\sigma_e = \sigma_1 - \sigma_2$	$\sigma_e = \sqrt{\sigma_1^2 + \sigma_2^2} - \sigma_1\sigma_2$

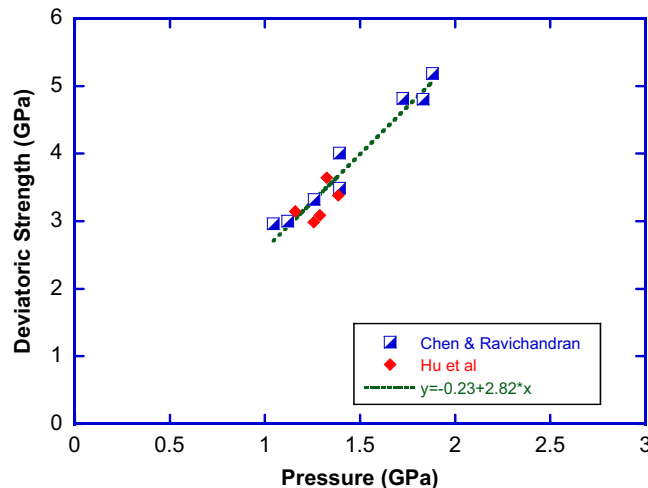


Fig. 9. Effect of pressure on deviatoric strength for confined dynamic experiments. The dashed line is the best linear fit to the existing data.

Chen and Ravichandran (2000) used the Mohr–Coulomb failure criterion to fit their triaxial confined data on aluminum nitride

$$|\tau| + \alpha p = \tau_0 \quad (4.1)$$

where τ is the maximum shear stress, p is the hydrostatic pressure, τ_0 is the shear strength when the pressure is zero and α is a fitting parameter (a material property). This approach can also be used to compare the triaxial/sleeve-based and planar confinement results, with $\tau_0=0.62$ GPa in the former case and $\tau_0=0.03$ GPa in the latter case. We define the maximum shear stress at the time of the peak stress as the “shear strength” of the material (note that this is different from the deviatoric strength defined previously). The results of the two techniques agree reasonably well using this approach as well, and the shear strength appears to change nearly linearly with the hydrostatic pressure for the range of pressures considered here, with $\alpha=1.34$ (compared to 0.93 for the Chen and Ravichandran (2000) data alone). The reason for difference of the fitting parameters is that we fit the high rate and low rate data together while Chen and Ravichandran fit the high strain rate data only. Thus our experimental results are broadly in agreement with those of Chen and Ravichandran in terms of strength. We will address the broader (and more fundamental) question of why the deviatoric and shear strengths are essentially linear with pressure in a later section. First, we compare the available experimental results over a broader range of pressures, and compare this to the existing phenomenological constitutive models for this material.

A much larger range of hydrostatic pressures can be achieved in plate impact (shock) experiments, where the state is essentially one of uniaxial strain, resulting in a stress state similar to that shown in Fig. 8(a). It is possible to compare these experiments with the triaxial/sleeve-based and planar confinement experiments using the equations provided in Table 1. All of the available experimental data on the confined behavior of aluminum nitride are presented in Fig. 10, including the results of uniaxial strain (plate impact) experiments from the work of Rosenberg et al. (1991) and Grady (1995) (as analyzed by Dandekar et al. (1994)). It is immediately apparent that the deviatoric strength of this material is not linearly dependent on pressure at the high pressures associated with the shock experiments. Indeed, a pressure-independent deviatoric strength is a better approximation of the behavior at high pressures below the phase transformation pressure, at which the wurtzite structure transforms to rocksalt structure (Kondo et al., 1982; Ueno et al., 1992; Vollstadt et al., 1990; Xia et al., 1993). For the results of Rosenberg et al. (1991), the deviatoric strength dependence on pressure is weak. The deviation from pressure insensitivity at very high pressures that Rosenberg et al. (1991) observed may be related with the phase transition in their specific material. Generally, the results of Rosenberg et al. (1991) and Grady are quantitatively different, but the dependence on pressure below the phase transition pressure is weak in either case. The analysis of Dandekar et al. (1994) suggested that “above the HEL it is not possible to verify the accuracy or fidelity of lateral stress measurements without knowing the properties of the material a priori.” Dandekar chose to use an equation of state based

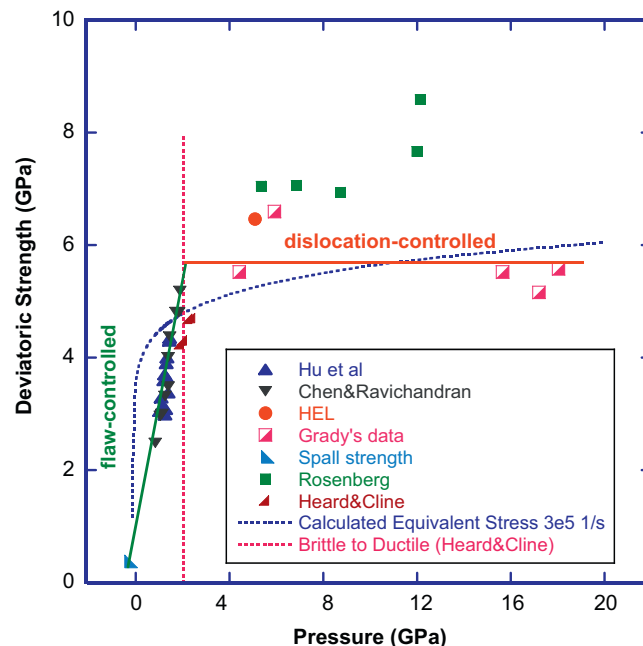


Fig. 10. All the available AlN data plotted in the deviatoric strength and pressure space. Note (i) Blue dashed curve shows the JH-2 model fit with Grady's shock data with $A=0.6432$, $N=0.1043$ and $C=0.0206$. (ii) Vertical dashed line corresponds to the pressure at which Heard and Cline observed the brittle to ductile transition. (iii) Two straight lines are drawn to illustrate the flaw-controlled region at low pressures and dislocation-controlled region at high pressures. (iv) Hu et al represents the current data; Chen&Ravichandran is from Chen and Ravichandran (1996); HEL and Rosenberg is from Rosenberg et al. (1991); Grady's data is from Dandekar et al. (1994); Spall strength is from Grady (1998); Heard&Cline is from Heard and Cline (1980).

on diamond-anvil cell experiments to extract the strength from the shock experiments of Grady. For the purpose of this discussion, we have chosen to simply use Dandekar's analysis of Grady's data, and note that the substance of the discussion remains valid using either the Grady data or the Rosenberg et al. (1991) data. In any case, the Mohr–Coulomb model is clearly not reasonable for high pressures (pressures above ~ 2 GPa), as noted by Chen and Ravichandran (2000).

The phenomenological constitutive model that is most commonly used to describe the high-strain-rate and high-pressure behavior of aluminum nitride is the Johnson–Holmquist-2 or JH-2 model, described specifically for this material by Holmquist et al. (2000; 2001) (a variant of this model, called the JHB model, addresses the high-pressure phase transformation of AlN and is described in (Johnson et al., 2003)). The JH-2 model essentially prescribes phenomenological pressure and rate-dependent behaviors for the undamaged (intact) ceramic and for the fully damaged (failed) ceramic, and prescribes an ad hoc damage evolution law for transitioning from the intact to the failed behaviors. The pressure-dependence in the model is power-law, and the rate-dependence is logarithmic. The behavior of the failed ceramic is constructed through an iterative procedure by attempting to match the results of computational simulations (using the model) of penetration with ballistic experiments. The parameters in the model are evaluated through a complex process described by Holmquist et al. (2001), using both laboratory experiments on constitutive behavior and ballistic experiments. We do not repeat the equations for the model here (they are presented in detail in Holmquist et al. (2001)), but show a comparison of that model (the dashed curve) with the experimental data in Fig. 10. The model is obviously unable to capture the experimental behavior, because the power-law function cannot match the low-pressure data and the shock data simultaneously. Chen and Ravichandran (2000) also pointed this out, and suggested that the high-pressure behavior (for which they used Rosenberg's rather than Grady's data) indicated a von Mises or Tresca type criterion associated with pressure insensitive plastic flow. However, they had no mechanistic evidence to prove this conjecture. We provide such evidence in this work.

Chen and Ravichandran (2000) attempted to understand the low-pressure behavior by assuming that the stress state at failure of the material was proportional to the stress at which wing cracks start to propagate. They concluded that the slope of the shear strength-pressure data at low pressures would then be determined entirely by the coefficient of friction μ on the sliding crack. However, Chen and Ravichandran also noted that the friction coefficient would have to be unreasonably high (at $\mu=1.13$) in order to obtain the measured slope of the strength-pressure data. They concluded, correctly, that their model was an oversimplification of the actual failure process (this is evident from our real-time photography in Fig. 7: the failures that have developed at the time of the compressive strength are not the long axial cracks expected from the simple wing-crack model). Further, $\mu=0.4$ for AlN according to the work of Tkachenko et al. (1983).

The available experimental data (using Grady's shock data rather than Rosenberg's), on the basis of Dandekar's analysis (1994) are also presented again in Fig. 10, where the focus is on the underlying deformation mechanisms. In Fig. 10, spall strength data (Grady, 1998) and uniaxial data (Chen and Ravichandran, 1996) are incorporated, and the deviatoric strength to pressure slope is around 2.2 by best linear fit. The brittle-to-ductile transition claimed by Heard and Cline (1980) occurred at a "confining pressure" of 0.55 GPa, which corresponds to a hydrostatic pressure of 2 GPa. A vertical line corresponding to this transition pressure is presented in Fig. 10, and it is immediately apparent that this line corresponds closely to the pressure at which a transition occurs in the behavior, from linearly pressure-dependent to essentially pressure-independent. One recognizes, of course, that the transition is not likely to be abrupt, but rather to occur in some range of pressures over which one mechanism begins to dominate another.

We hypothesize that the pressure-dependent behavior below the transition pressure is the result of the interaction of large numbers of wing cracks developed from pre-existing flaws (defects) inside the material (this interaction is described rigorously by Paliwal and Ramesh (2008)). The compressive strength (and thence the deviatoric strength) is dependent on the defect distribution, the rate of loading, and the crack dynamics, as well as the intrinsic material properties (elastic moduli, fracture toughness, density) and the coefficient of friction, as has been shown previously (Denoual and Hild, 2000, 2002; Espinosa, 1995; Espinosa and Brar, 1995; Espinosa et al., 1992, 1998; Forquin et al., 2003; Hild et al., 2003; Zavattieri and Espinosa, 2001). We call the behavior in this region *flaw-controlled*. Above the transition pressure, we hypothesize that the pressure-insensitive behavior is the result of dislocation-driven plastic flow, and call the behavior in this region *dislocation-controlled*.

Evidence for the flaw-controlled brittle failure mechanism in aluminum nitride is abundant in the literature and in our own experiments in terms of post-mortem analysis of fragments, but our high-speed real-time visualization demonstrates for the first time that brittle damage processes occur in aluminum nitride during the dynamic loading phase and not just during the unloading. Further, such an elastic-brittle failure mechanism must result in deviatoric strengths that are linearly dependent on the hydrostatic pressure. Consider the plane strain elastic-brittle case, with the applied compressive stress σ_1 and the applied confining stress as σ_2 . The third confining stress σ_3 is prescribed by the plane strain condition

$$\sigma_3 = \nu(\sigma_1 + \sigma_2) \quad (4.2)$$

The stress intensity factor associated with a given wing crack is given by Ashby and Hallam (1986)

$$K_I = -\frac{\sqrt{\pi a}}{(1+L)^{3/2}} \left[0.23L + \frac{1}{\sqrt{3}(1+L)^{1/2}} \right] [\sigma_1 - \sigma_2 - \mu(\sigma_1 + \sigma_2) - 4.3\sigma_2 L] \quad (4.3)$$

where the normalized wing crack length is $L=l/a$, the preexisting flaw size is $2a$ and μ is the coefficient of friction. This equation provides the relationship between the applied confining stress σ_2 and the compressive stress σ_1 for the onset of

crack growth since K_{IC} is known. The latter two equations will allow us to compute the equivalent stress σ_e as

$$\sigma_e = \sqrt{\frac{1}{2} [(\sigma_1 - \sigma_2)^2 + (\sigma_2 - \sigma_3)^2 + (\sigma_3 - \sigma_1)^2]} \tag{4.4}$$

as well as the corresponding hydrostatic pressure (both in terms of σ_1). The result is

$$\begin{aligned} \sigma_e^2 &= \sigma_1^2 [v^2(\alpha^2 + 2\alpha) - v(\alpha^2 + 2\alpha) + 1] \\ &+ \sigma_1 \beta [v^2(2\alpha + 2) - v(2\alpha + 2) + 2\alpha - 1] + \beta^2 (v^2 - v + 1) \end{aligned} \tag{4.5}$$

and

$$p = (1 + v)[(1 + \alpha)\sigma_1 + \beta]/3 \tag{4.6}$$

where

$$\alpha = \frac{1 - \mu}{1 + \mu + 4.3L} \tag{4.7}$$

and

$$\beta = \frac{K_{IC}(1 + L)^{3/2}}{\sqrt{\pi a}} (1 + \mu + 4.3L)[0.23L + (1)/(\sqrt{3}(1 + L)^{1/2})] \tag{4.8}$$

We can now compute the slope of the straight line in an deviatoric strength-pressure plot (such as that in Fig. 10). The slope will depend on σ_1 as well as on the friction coefficient μ , Poisson's ratio v , fracture toughness K_{IC} , and the normalized wing crack length L . However, it turns out that this slope is comparatively insensitive to the compressive strength (σ_1) of the material, as well as to the friction coefficient, the pre-existing flaw size, the normalized wing crack length and the fracture toughness. However, the slope is strongly sensitive to the Poisson's ratio, see Fig. 11. For the particular case of AlN with a Poisson's ratio of 0.237, the slope must be approximately 2.2. This is in fact very close to what is observed for aluminum nitride in the flaw-controlled region, demonstrating that the behavior here is essentially elastic-brittle. A straight line with that slope is shown in Fig. 10. Note that the line passes through the one tensile result available, the spall data of Grady (1998).

What causes the change in mechanism at high pressures? While it is possible that a new deformation mechanism is triggered for the first time at high pressures, it is certain that the flaw-controlled brittle failure mechanism is shut down at sufficiently high pressures. The wing-crack mechanism is not feasible when the stress intensity factor at the flaw tip (for the biaxial case) goes to zero (Ashby and Hallam, 1986; Horii and Nemat-Nasser, 1986):

$$K_I = \sqrt{\frac{\pi a}{3}} \left\{ (\sigma_2 - \sigma_1) \sqrt{1 + \mu^2} + \mu(\sigma_2 + \sigma_1) \right\} = 0 \tag{4.9}$$

Under this condition, none of the flaws will be able to activate the wing crack mechanism, irrespective of flaw size. This relationship implies that for any applied axial stress σ_1 , one can shut down the initiation of wing cracks by applying a

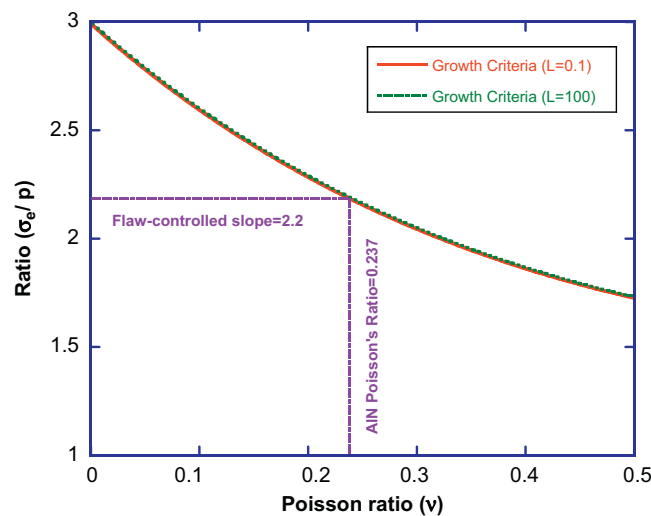


Fig. 11. Effect of Poisson's ratio on the ratio of deviatoric strength over pressure for the plain strain condition using the wing crack growth criteria at different L . Note (i) The normalized wing crack length does not have a strong effect on the σ_e/p ratio. (ii) As the Poisson's ratio approaches zero, the ratio should approach 3 by the definition of the pressure and equivalent stress. (iii) The Poisson's ratio for AlN is 0.237, giving a σ_e/p of 2.2 at the crack dominant region.

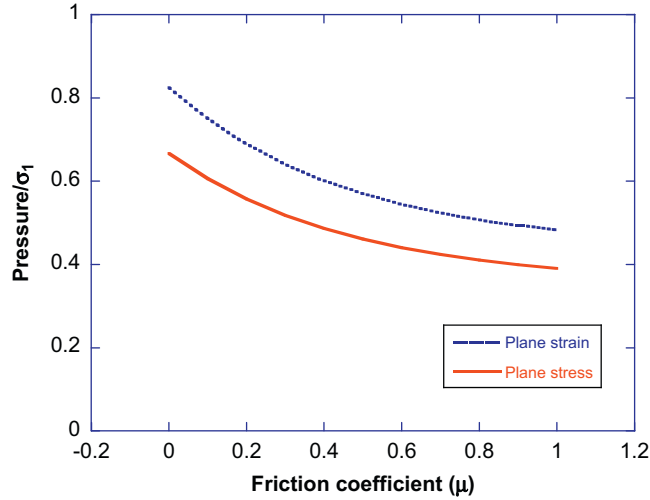


Fig. 12. Normalized crack shut-down pressure as a function of friction coefficient for both plane strain and plain stress conditions (Poisson's ratio $\nu=0.237$).

transverse stress σ_2 that is sufficiently large to satisfy Eq. (4.9), i.e., when

$$\sigma_2 = c\sigma_1 \quad (4.10)$$

where

$$c = \frac{(1+\mu^2)^{1/2} - \mu}{(1+\mu^2)^{1/2} + \mu} \quad (4.11)$$

In the case of plane strain, we are able to compute σ_2 , and thence to compute the pressure required to shut down the wing crack mechanism for a given applied axial stress σ_1 . This “shut-down pressure” is given by

$$p = \frac{2(1+\nu)(1+\mu^2)^{1/2}}{3(1+\mu^2)^{1/2} + \mu} \sigma_1 \quad (4.12)$$

The normalized shut down pressure is plotted as a function of friction coefficient μ in Fig. 12 for both plain strain and plane stress cases. For the particular case of aluminum nitride, given the Poisson's ratio $\nu=0.237$ and coefficient of friction $\mu=0.4$ (Tkachenko et al., 1983), and with the applied axial stress in the Heard and Cline (and most other) experiments being of the order of 4 GPa, we see that the shut-down pressure should be of the order of 2.5 GPa. This simplistic estimate is remarkably close to the pressure at which the apparent brittle to ductile transition is observed in AlN (Fig. 10), suggesting that the shutdown of wing-crack activation plays a role in this transition. Other mechanisms must take over to determine the strength for all higher pressures and now we show here that in AlN dislocation mechanisms are active at the higher pressures.

Note that current shut down pressure analysis above does not account for the presence of a second phase at some of the grain boundaries. Espinosa and coworkers (Espinosa, 1995; Espinosa et al., 1998) showed that the existence of a second phase at the grain boundaries can affect parameters, such as the local internal friction coefficient μ and critical stress intensity factor K_{IC} . However, in this AlN the second phase does not exist along all grain boundaries (see Fig. 2b and c), and so the effects of the second phase will be comparatively weak. A simple first-order homogenization analysis has been carried out to estimate the effect of the yttria on the effective internal friction coefficient and the effective strength. This analysis shows that the quantitative effect on the computed shut-down pressure is less than 5%.

Our evidence for the dislocation-controlled region is both macroscopic (the pressure-insensitive behavior) and microscopic (through TEM studies). Note that there has some TEM characterization of the deformation mechanisms under high strain rate loading conditions, e.g., Espinosa et al. (1992). The as-received aluminum nitride material contained no visible dislocations in any of the multiple locations that we investigated in the TEM (see Fig. 2). However, 20–30% of the multiple locations examined after dynamic loading under the maximum confining stress (780 MPa, corresponding to a hydrostatic pressure of 1.5 GPa) show a high density of dislocations. A typical example is shown in the dark-field TEM of Fig. 13a compared with the as-received material microstructure at the same zone axis (Fig. 2a), with high-density arrays of dislocations (shown also in Fig. 13b–d). Thus dislocation networks are generated during the confined experiments, and contribute to the global deformation. The dislocations observed have a Burger's vector of $(1/3)[1\bar{2}10]$ and the active slip system are the slip systems $(0001)\langle 1\bar{2}10 \rangle$ and $\{10\bar{1}0\}\langle 1\bar{2}10 \rangle$, similar to the dislocations observed by Heard and Cline (1980) at high pressures and by Audurier et al. (1998) and Feregotto et al., (1997) at high temperatures. Thus the dislocation plasticity mechanism seems operational and viable at high pressures in our confined experiments. In general,

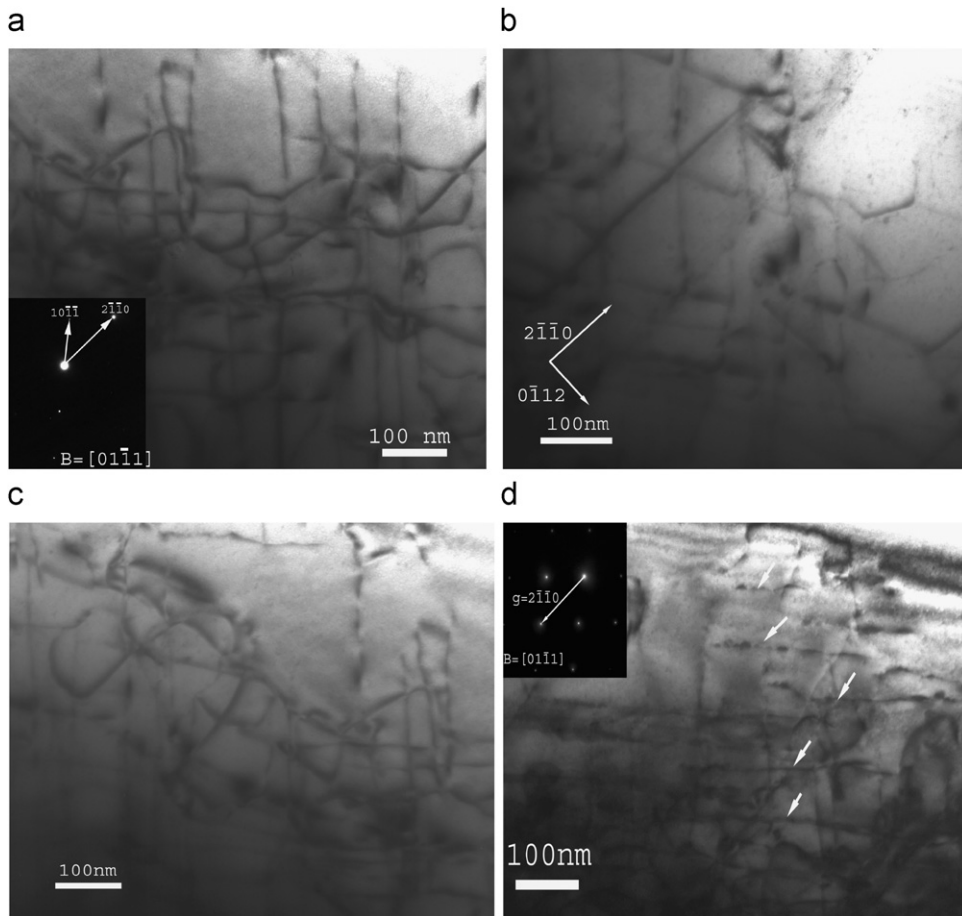


Fig. 13. TEM pictures show multiple positions of dynamically deformed AlN at pressure around 1.5 GPa, with the same zone axis of $[01\bar{1}1]$. The dislocations observed have a Burger's vector of $(1/3)[1\bar{2}10]$ and the active slip systems are $(0001)\langle 1\bar{2}10\rangle$ and $\{10\bar{1}0\}\langle 1\bar{2}10\rangle$.

dislocations are easily seen in our deformed samples after confined deformations (Fig. 13), while we have not been able to observe any dislocations in our as received samples (Fig. 2).

Since the brittle fracture mechanism is necessarily shut down at sufficiently high pressures (because the K_I at the crack tips tends to zero), the dislocation mechanism must become more and more dominant (in terms of dislocation nucleation and mobility) as the pressure increases. This is the essence of the transition region, a similar argument is invoked by Deshpande and Evans (2008).

We note that we have not been able to obtain post-mortem samples of shock-loaded aluminum nitride for TEM evaluation to establish that the dislocation mechanism was also active in those experiments (the shock experiments were performed nearly twenty years ago, and samples were not retained). The cost of performing a full range of new shock experiments is extremely high, but we will pursue such results and the associated TEM in a future work.

In summary, the constitutive behavior of aluminum nitride can be summarized as below. In the low pressure range (below 2 GPa), i.e., the defect controlled region, the behavior can be expressed as

$$\sigma_e = 0.75 + 2.23p \quad (p \leq 2 \text{ GPa}) \quad (4.13)$$

In the high pressure range (above 3 GPa), i.e., the dislocation controlled region

$$\sigma_e = 5.7(p \geq 3 \text{ GPa}) \quad (4.14)$$

The transition from the defect controlled region to the dislocation controlled region is likely to occur over a range of pressures. One possible description of the transition region is,

$$\sigma_e = -0.49p^2 + 2.94p + 1.29 \quad (2 \text{ GPa} \leq p \leq 3 \text{ GPa}) \quad (4.15)$$

which matches the two fundamental mechanisms. This mechanism-based constitutive description gives a good representation of the available experimental data, as shown in Fig. 14.

Under loading, below the transition pressure, the failure envelop is essentially elastic. As pressure increases, the failure of AlN is determined by the deviatoric strength and pressure envelop. Such a mechanism based constitutive model idea is

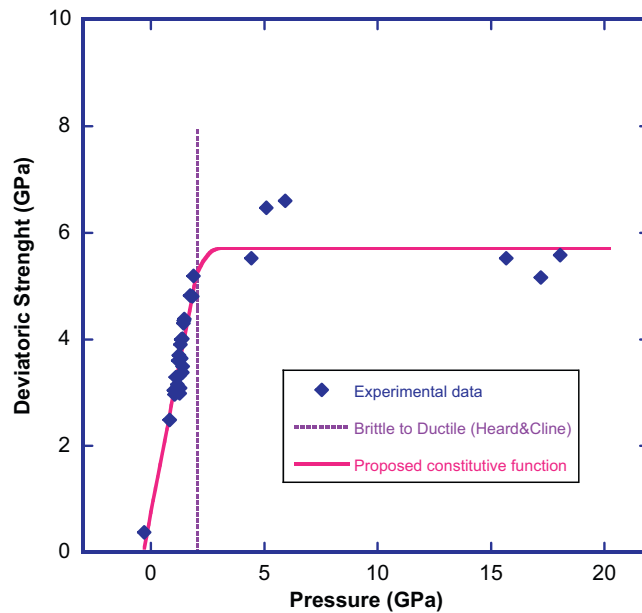


Fig. 14. Proposed constitutive description of AlN based upon the different mechanisms activated at different pressures. Experimental data are the same data as in Fig. 10.

similar to that sometimes adopted in concrete research where a crack model is used to bound the tensile stresses and a damaged plasticity model is used to capture the compressive strengths, e.g. [Feenstra and deBorst \(1996\)](#).

5. Conclusions

We have conducted quasistatic, dynamic and dynamic confined experiments on aluminum nitride with simultaneous real-time high-speed visualization of the failure processes, and performed detailed microscopic characterization of the deformed and fragmented samples. A mechanism based failure envelop is proposed for AlN, and has implications for other brittle solids with brittle-ductile transition behavior. The results can be summarized as follows:

- The compressive strength of the sintered AlN is sensitive to strain rate over the strain rate range of 10^{-3} – 10^3 s $^{-1}$, consistent with previous experimental data.
- Direct visualization of the confined failure process is obtained through the combination of a planar confinement technique and high speed visualization. The failure pattern under confined dynamic loading is different from that under uniaxial dynamic loading, indicating a stronger influence of shear under confinement.
- Comparing all of the available experimental data on AlN, the wing crack model is employed to describe the slope of equivalent stress to pressure and to compute a shut-down pressure for the cracking mechanism, consistent with experimental observation.
- TEM characterization of the as-received material and of fragments from the dynamic experiments has been performed. In general, dislocations are easily seen in our deformed samples after confined deformation ([Fig. 13](#)), while we have not been able to observe any dislocations in our as received samples ([Fig. 2](#)).

Acknowledgements

This work was performed under the auspices of the Center for Advanced Metallic and Ceramic Systems (CAMCS) at the Johns Hopkins University, supported by the Army Research Laboratory under the ARMAC-RTP Cooperative Agreement Nos. DAAD19-01-2-0003 and W911NF-06-2-0006.

References

- Ashby, M.F., Hallam, S.D., 1986. The failure of brittle solids containing small cracks under compressive stress states. *Acta Metallurgica* 34 (3), 497–510.
- Audurier, V., Demenet, J.L., Rabier, J., 1998. AlN plastic deformation between room temperature and 800 C. I. Dislocation substructure observations. *Philosophical Magazine A* 77 (4), 825–842.
- Baik, Y., Drew, R.A.L., 1996. Aluminum nitride: processing and applications. *Advanced Ceramic Materials* 122, 553–570.

- Bhattacharya, K., Ortiz, M., Ravichandran, G., 1998. Energy-based model of compressive splitting in heterogeneous brittle solids. *Journal of the Mechanics and Physics of Solids* 46 (10), 2171–2181.
- Bombolakis, E.G., 1973. Study of the brittle fracture process under uniaxial compression. *Tectonophysics* 18 (3–4), 231–248.
- Brace, W.F., Bombolakis, E.G., 1963. A note on brittle crack growth in compression. *Journal of Geophysical Research* 68 (12), 3709–3713.
- Branicio, P.S., Kalia, R.K., Nakano, A., Vashishta, P., 2006. Shock-induced structural phase transition, plasticity, and brittle cracks in aluminum nitride ceramic. *Physical Review Letters* 96, 6.
- Bu, G., Ciplys, D., Shur, M., Schowalter, L.J., Schujman, S., Gaska, R., 2004. Electromechanical coupling coefficient for surface acoustic waves in single-crystal bulk aluminum nitride. *Applied Physics Letters* 84 (23), 4611–4613.
- Chen, W., Ravichandran, G., 2000. Failure mode transition in ceramics under dynamic multiaxial compression. *International Journal of Fracture* 101 (1–2), 141–159.
- Chen, W.N., Ravichandran, G., 1996. Static and dynamic compressive behavior of aluminum nitride under moderate confinement. *Journal of the American Ceramic Society* 79 (3), 579–584.
- Chen, W.N., Ravichandran, G., 1997. Dynamic compressive failure of a glass ceramic under lateral confinement. *Journal of the Mechanics and Physics of Solids* 45 (8), 1303–1328.
- Chen, W.W., Rajendran, A.M., Song, B., Nie, X., 2007. Dynamic fracture of ceramics in armor applications. *Journal of the American Ceramic Society* 90 (4), 1005–1018.
- Dandekar, D.P., Abbate, A., Frankel, J., 1994. Equation of state of aluminum nitride and its shock response. *Journal of Applied Physics* 76 (7), 4077–4085.
- Denoual, C., Hild, F., 2000. A damage model for the dynamic fragmentation of brittle solids. *Computer Methods in Applied Mechanics and Engineering* 183 (3–4), 247–258.
- Denoual, C., Hild, F., 2002. Dynamic fragmentation of brittle solids: a multi-scale model. *European Journal of Mechanics—A/Solids* 21 (1), 105–120.
- Deshpande, V.S., Evans, A.G., 2008. Inelastic deformation and energy dissipation in ceramics: a mechanism-based constitutive model. *Journal of the Mechanics and Physics of Solids* 56 (10), 3077–3100.
- Dubois, M.A., Muralt, P., 1999. Properties of aluminum nitride thin films for piezoelectric transducers and microwave filter applications. *Applied Physics Letters* 74 (20), 3032–3034.
- Espinosa, H.D., 1995. On the dynamic shear resistance of ceramic composites and its dependence on applied multiaxial deformation. *International Journal of Solids and Structures* 32 (21), 3105–3128.
- Espinosa, H.D., Brar, N.S., 1995. Dynamic failure mechanisms of ceramic bars: Experiments and numerical simulations. *Journal of the Mechanics and Physics of Solids* 43 (10), 1615–1619.
- Espinosa, H.D., Raiser, G., Clifton, R.J., Ortiz, M., 1992. Experimental observations and numerical modeling of inelasticity in dynamically loaded ceramics. *Journal of Hard Materials* 3, 285–313.
- Espinosa, H.D., Zavattieri, P.D., Dwivedi, S.K., 1998. A finite deformation continuum discrete model for the description of fragmentation and damage in brittle materials. *Journal of the Mechanics and Physics of Solids* 46 (10), 1909–1942.
- Feenstra, P.H., deBorst, R., 1996. A composite plasticity model for concrete. *International Journal of Solids and Structures* 33 (5), 707–730.
- Feregotto, V., George, A., Michel, J.P., 1997. Dislocations and extended defects in AlN deformed at high temperatures. *Materials Science and Engineering a-Structural Materials Properties Microstructure and Processing* 234, 625–628.
- Forquin, P., Denoual, C., Cottenot, C.E., Hild, F., 2003. Experiments and modelling of the compressive behaviour of two SiC ceramics. *Mechanics of Materials* 35 (10), 987–1002.
- Grady, D.E., 1995. Shock Properties of High-Strength Ceramics. Sandia National Lab., Experimental Impact Physics Department, Albuquerque, New Mexico.
- Grady, D.E., 1998. Shock-wave compression of brittle solids. *Mechanics of Materials* 29 (3–4), 181–203.
- Heard, H., Cline, C., 1980. Mechanical behavior of polycrystalline BeO, Al₂O₃ and AlN at high-pressure. *Journal of Material Science* 15 (8), 1889–1897.
- Hild, F., Denoual, C., Forquin, P., Brajer, X., 2003. On the probabilistic-deterministic transition involved in a fragmentation process of brittle materials. *Computers and Structures* 81 (12), 1241–1253.
- Hoek, E., Bieniawski, Z.T., 1984. Brittle-fracture propagation in rock under compression. *International Journal of Fracture* 26 (4), 276–294.
- Holmquist, T.J., Templeton, D.W., Bishnoi, K.D., 2000. High strain rate constitutive modeling of aluminum nitride including a first-order phase transformation. *J. Phys. IV* 10, 21–26 France Pr. 9 (DYMAT 2000).
- Holmquist, T.J., Templeton, D.W., Bishnoi, K.D., 2001. Constitutive modeling of aluminum nitride for large strain, high-strain rate, and high-pressure applications. *International Journal of Impact Engineering* 25 (3), 211–231.
- Horii, H., Nemat-Nasser, S., 1985. Compression-induced microcrack growth in brittle solids: axial splitting and shear failure. *J. Geophys. Res.*, 90.
- Horii, H., Nemat-Nasser, S., 1986. Brittle failure in compression: splitting, faulting and brittle–ductile transition. *Phil. Trans. R. Soc. Lond. A* 319, 1549.
- Huang, C.Y., Subhash, G., 2003. Influence of lateral confinement on dynamic damage evolution during uniaxial compressive response of brittle solids. *Journal of the Mechanics and Physics of Solids* 51 (6), 1089–1105.
- Jiao, T., Li, Y.L., Ramesh, K.T., Wereszczak, A.A., 2004. High rate response and dynamic failure of structural ceramics. *International Journal of Applied Ceramic Technology* 1 (3), 243–253.
- Johnson, G.R., Holmquist, T.J., Beissel, S.R., 2003. Response of aluminum nitride (including a phase change) to large strains, high strain rates, and high pressures. *Journal of Applied Physics* 94 (3), 1639–1646.
- Kipp, M.E., Grady, D.E., 1994. Shock phase-transformation and release properties of aluminum nitride. In: *Proceedings of the International Conference on Mechanical and Physical Behaviour of Materials under Dynamic Loading (EURODYMAT 94)*. Editions Physique, Oxford, England, pp. 249–256.
- Kondo, K., Sawaoka, A., Sato, K., Ando, M., 1982. Shock compression and phase transformation of AlN and BP. *AIP Conference Proceedings* 78 (1), 325–329.
- Lankford, J., Predebon, W.W., Staehler, J.M., Subhash, G., Pletka, B.J., Anderson, C.E., 1998. The role of plasticity as a limiting factor in the compressive failure of high strength ceramics. *Mechanics of Materials* 29 (3–4), 205–218.
- Lawn, B.R., Padture, N.P., Cai, H.D., Guiberteau, F., 1994. Making ceramics ductile. *Science* 263 (5150), 1114–1116.
- Martin, P.M., Good, M.S., Johnston, J.W., Posakony, G.J., Bond, L.J., Crawford, S.L., 2000. Piezoelectric films for 100-MHz ultrasonic transducers. *Thin Solid Films* 379 (1–2), 253–258.
- Nakamura, A., Mashimo, T., 1994. Shock-induced phase transition of AlN. In: Schmidt, S.C., Shaner, J.W., Samara, G.A., Ross, M. (Eds.), *High Pressure Science and Technology 1993*. American Institute of Physics, New York, pp. 303–306.
- Nemat-Nasser, S., Deng, H., 1994. Strain-rate effect on brittle failure in compression. *Acta Metallurgica Et Materialia* 42 (3), 1013–1024.
- Nemat-Nasser, S., Horii, H., 1982. Compression-induced nonplanar crack extension with application to splitting, exfoliation, and rockburst. *Journal of Geophysical Research*, 87.
- Orphal, D.L., Franzen, R.R., Piekutowski, A.J., Forrestal, M.J., 1996. Penetration of confined aluminum nitride targets by tungsten long rods at 1.5–4.5 km/s. *International Journal of Impact Engineering* 18 (4), 355–368.
- Paliwal, B., Ramesh, K.T., 2007. Effect of crack growth dynamics on the rate-sensitive behavior of hot-pressed boron carbide. *Scripta Materialia* 57 (6), 481–484.
- Paliwal, B., Ramesh, K.T., 2008. An interacting micro-crack damage model for failure of brittle materials under compression. *Journal of the Mechanics and Physics of Solids* 56 (3), 896–923.
- Paliwal, B., Ramesh, K.T., McCauley, J.W., 2006. Direct observation of the dynamic compressive failure of a transparent polycrystalline ceramic (AlON). *Journal of the American Ceramic Society* 89 (7), 2128–2133.
- Paliwal, B., Ramesh, K.T., McCauley, J.W., Chen, M.W., 2008. Dynamic compressive failure of ALON under controlled planar confinement. *Journal of the American Ceramic Society* 91 (11), 3619–3629.

- Rafaniello, W., Zhao, J., Haney, C., The effect of process changes on the ballistic performance of sintered aluminum nitride, unpublished.
- Ravichandran, G., Subhash, G., 1994. Critical-appraisal of limiting strain rates for compression testing of ceramics in a split hopkinson pressure bar. *Journal of the American Ceramic Society* 77 (1), 263–267.
- Ravichandran, G., Subhash, G., 1995. A micromechanical model for high-strain rate behavior of ceramics. *International Journal of Solids and Structures* 32 (17–18), 2627–2646.
- Rhee, Y.-W., Kim, H.-W., Deng, Y., Lawn, B.R., 2001. Brittle fracture versus quasi plasticity in ceramics: a simple predictive index. *Journal of the American Ceramic Society* 84 (3), 561–565.
- Rosenberg, Z., Brar, N.S., Bless, S.J., 1991. Dynamic high-pressure properties of aln ceramic as determined by flyer plate impact. *Journal of Applied Physics* 70 (1), 167–169.
- Schulson, E.M., 1990. The brittle compressive fracture of ice. *Acta Metallurgica Et Materialia* 38 (10), 1963–1976.
- Subhash, G., Ravichandran, G., 1998. Mechanical behaviour of a hot pressed aluminum nitride under uniaxial compression. *Journal of Material Science* 33 (7), 1933–1939.
- Subhash, G., Ravichandran, G., 2000. Split-Hopkinson Pressure Bar Testing of Ceramics. ASM International, Materials Park, OH.
- Tkachenko, Y.G., Yulyugin, V.K., Dubovik, T.V., 1983. Effect of temperature and environment on the friction and wear of aluminum nitride. *Powder Metallurgy and Metal Ceramics* 22 (5), 405–406.
- Trolier-McKinstry, S., Murali, P., 2004. Thin film piezoelectrics for MEMS. *Journal of Electroceramics* 12 (1-2), 7–17.
- Ueno, M., Onodera, A., Shimomura, O., Takemura, K., 1992. X-Ray-observation of the structural phase-transition of aluminum nitride under high-pressure. *Physical Review B* 45 (17), 10123–10126.
- Vollstadt, H., Ito, E., Akaishi, M., Akimoto, S., Fukunaga, O., 1990. High-pressure synthesis of rock-salt type of AlN. *Proceedings of the Japan Academy Series B-Physical and Biological Sciences* 66 (1), 7–9.
- Wang, H., Ramesh, K.T., 2004. Dynamic strength and fragmentation of hot-pressed silicon carbide under uniaxial compression. *Acta Materialia* 52 (2), 355–367.
- Xia, Q., Xia, H., Ruoff, A.L., 1993. Pressure-induced rocksalt phase of aluminum nitride: a metastable structure at ambient condition. *Journal of Applied Physics* 73 (12), 8198–8200.
- Zavattieri, P.D., Espinosa, H.D., 2001. Grain level analysis of crack initiation and propagation in brittle materials. *Acta Materialia* 49 (20), 4291–4311.
- Zheng, L., Ramalingam, S., Shi, T., Peterson, R.L., 1993. Aluminum nitride thin-film sensor for force, acceleration, and acoustic-emission sensing. *Journal of Vacuum Science & Technology a-Vacuum Surfaces and Films* 11 (5), 2437–2446.

NO. OF
COPIES ORGANIZATION

1 DEFENSE TECHNICAL
(PDF INFORMATION CTR
only) DTIC OCA
8725 JOHN J KINGMAN RD
STE 0944
FORT BELVOIR VA 22060-6218

1 DIRECTOR
US ARMY RESEARCH LAB
IMNE ALC HRR
2800 POWDER MILL RD
ADELPHI MD 20783-1197

1 DIRECTOR
US ARMY RESEARCH LAB
RDRL CIO LL
2800 POWDER MILL RD
ADELPHI MD 20783-1197

NO. OF
COPIES ORGANIZATION

1 PEO GCS
SFAE GCS BCT/MS 325
M RYZYI
6501 ELEVEN MILE RD
WARREN MI 48397-5000

1 ABRAMS TESTING
SFAE GCSS W AB QT
J MORAN
6501 ELEVEN MILE RD
WARREN MI 48397-5000

1 COMMANDER
WATERVLIET ARSENAL
SMCWV QAE Q
B VANINA
BLDG 44
WATERVLIET NY 12189-4050

1 COMMANDER
US ARMY AMCOM
AVIATION APPLIED TECH DIR
J SCHUCK
FT EUSTIS VA 23604-5577

1 USA SBCCOM PM SOLDIER SPT
AMSSB PM RSS A
J CONNORS
KANSAS ST
NATICK MA 01760-5057

1 UNIV OF DELAWARE
DEPT OF MECH ENGR
J GILLESPIE
NEWARK DE 19716

3 AIR FORCE ARMAMENT LAB
AFATL DLJW
D BELK
J FOSTER
W COOK
EGLIN AFB FL 32542

1 TACOM ARDEC
AMSRD AAR AEE W
E BAKER
BLDG 3022
PICATINNY ARSENAL NJ
07806-5000

NO. OF
COPIES ORGANIZATION

11 US ARMY TARDEC
AMSTRA TR R MS 263
K BISHNOI
D TEMPLETON (10 CPS)
WARREN MI 48397-5000

1 COMMANDER
US ARMY RSRCH OFC
A RAJENDRAN
PO BOX 12211
RSRCH TRIANGLE PARK NC
27709-2211

2 CALTECH
G RAVICHANDRAN
T AHRENS MS 252 21
1201 E CALIFORNIA BLVD
PASADENA CA 91125

5 SOUTHWEST RSRCH INST
C ANDERSON
K DANNEMANN
T HOLMQUIST
G JOHNSON
J WALKER
PO DRAWER 28510
SAN ANTONIO TX 78284

3 SRI INTERNATIONAL
D CURRAN
D SHOCKEY
R KLOOP
333 RAVENSWOOD AVE
MENLO PARK CA 94025 21

1 APPLIED RSRCH ASSOCIATES
D GRADY
4300 SAN MATEO BLVD NE
STE A220
ALBUQUERQUE NM 87110

1 INTERNATIONAL RSRCH
ASSOCIATES INC
D ORPHAL CAGE 06EXO
5274 BLACKBIRD DR
PLEASANTON CA 94566

1 BOB SKAGGS CONSULTANT
S R SKAGGS
7 CAMINO DE LOS GARDUNOS
SANTA FE NM 87506

NO. OF
COPIES ORGANIZATION

2 WASHINGTON ST UNIV
INST OF SHOCK PHYSICS
Y GUPTA
J ASAY
PULLMAN WA 99164-2814

1 COORS CERAMIC CO
T RILEY
600 NINTH ST
GOLDEN CO 80401

1 UNIV OF DAYTON
RSRCH INST
N BRAR
300 COLLEGE PARK
MS SPC 1911
DAYTON OH 45469-0168

1 COMMANDER
US ARMY TACOM
AMSTA TR S
L PROKURAT FRANKS
WARREN MI 48397-5000

1 PM HBCT
SFAE GCS HBCT S
J ROWE MS 506
6501 11 MILE RD
WARREN MI 48397-5000

3 COMMANDER
US ARMY RSRCH OFC
B LAMATINA
D STEPP
W MULLINS
PO BOX 12211
RSRCH TRIANGLE PARK NC
27709-2211

1 NAVAL SURFACE WARFARE CTR
CARDEROCK DIVISION
R PETERSON
CODE 28
9500 MACARTHUR BLVD
WEST BETHESDA MD 20817-5700

2 LAWRENCE LIVERMORE NATL LAB
R LANDINGHAM L369
J E REAUGH L282
PO BOX 808
LIVERMORE CA 94550

NO. OF
COPIES ORGANIZATION

3 SANDIA NATL LAB
J ASAY MS 0548
L CHHABILDAS MS 0821
D CRAWFORD ORG 0821
PO BOX 5800
ALBUQUERQUE NM 87185-0820

1 RUTGERS
THE STATE UNIV OF NEW JERSEY
DEPT OF CRMCS & MATLS ENGRNG
R HABER
607 TAYLOR RD
PICATINNY NJ 08854

1 THE UNIVERSITY OF TEXAS
AT AUSTIN
S BLESS
IAT
3925 W BRAKER LN STE 400
AUSTIN TX 78759-5316

1 CERCOM
R PALICKA
1960 WATSON WAY
VISTA CA 92083

6 GDLS
W BURKE MZ436 21 24
G CAMPBELL MZ436 30 44
D DEBUSSCHER MZ436 20 29
J ERIDON MZ436 21 24
W HERMAN MZ435 01 24
S PENTESCU MZ436 21 24
38500 MOUND RD
STERLING HTS MI 48310-3200

1 JET PROPULSION LAB
IMPACT PHYSICS GROUP
M ADAMS
4800 OAK GROVE DR
PASADENA CA 91109-8099

3 OGARA HESS & EISENHARDT
G ALLEN
D MALONE
T RUSSELL
9113 LE SAINT DR
FAIRFIELD OH 45014

NO. OF
COPIES ORGANIZATION

NO. OF
COPIES ORGANIZATION

1 CERADYNE INC
M NORMANDIA
3169 REDHILL AVE
COSTA MESA CA 96626

2 JOHNS HOPKINS UNIV
DEPT OF MECH ENGRNG
K T RAMESH
T W WRIGHT
3400 CHARLES ST
BALTIMORE MD 21218

2 SIMULA INC
V HORVATICH
V KELSEY
10016 51ST ST
PHOENIX AZ 85044

3 UNITED DEFENSE LP
K STRITTMATTER
E BRADY
R JENKINS
PO BOX 15512
YORK PA 17405-1512

10 NATL INST OF STANDARDS & TECH
CRMCS DIV
G QUINN
STOP 852
GAITHERSBURG MD 20899

2 DIR USARL
RDRL D
C CHABALOWSKI
V WEISS
2800 POWDER MILL RD
ADELPHI MD 20783-1197 23

ABERDEEN PROVING GROUND

60 DIR USARL
RDRL SL
R COATE
RDRL WM
S KARNA
P BAKER
J MCCAULEY (10 CPS)
RDRL WML
J NEWILL
M ZOLTOSKI
RDRL WML B
D TAYLOR (10 CPS)
RDRL WMM
R DOWDING

RDRL WMM A
J SANDS
T WEERASOORIYA
RDRL WMM D
E CHIN
K CHO
G GAZONAS
R SQUILLACIOTI
RDRL WMM E
J LASALVIA
P PATEL
RDRL WMM F
J MONTGOMERY
RDRL WMP
B BURNS
S SCHOENFELD
RDRL WMP B
C HOPPEL
M SCHEIDLER
RDRL WMP C
T BJERKE
J CLAYTON
D DANDEKAR
M GREENFIELD
S SEGLETES
W WALTERS
RDRL WMP D
T HAVEL
M KEELE
D KLEPONIS
H MEYER
J RUNYEON
RDRL WMP E
P BARTKOWSKI
M BURKINS
W GOOCH
D HACKBARTH
E HORWATH
T JONES
RDRL WML H
T FARRAND
L MAGNESS
D SCHEFFLER
R SUMMERS

INTENTIONALLY LEFT BLANK.